Tungsten as First Wall Material in ASDEX Upgrade

R. Dux, R. Neu, V. Bobkov, H. Greuner, O. Gruber, A. Herrmann, A. Kallenbach, C. Maggi, T. Pütterich, V. Rohde and ASDEX Upgrade Team

Max-Planck-Institut für Plasmaphysik, EURATOM Association, D-85748 Garching
e-mail: Ralph.Dux@ipp.mpg.de

Abstract In ASDEX Upgrade, nearly all plasma facing components (PFC) besides the strike point area of the lower divertor are tungsten coated. The main, newly added components are the low field side (LFS) poloidal guard limiters, the roof baffle in the lower divertor and the lower passive stabiliser loop. The increased W-area resulted in higher W concentrations in the plasma. Especially the LFS limiters represent a significant W source mainly during ICRF operation, which is probably due to a rise of the sheath potential. NBI leads to sputtering by fast D^+ ions. The fast ion loss is enhanced by ELMs. In H-modes with type-I ELMs, about 70% of the local W-influx at the middle of the limiter appears during ELMs. During the ELM the mean energy of the ions hitting the W-surface is increased, which is the predominant contribution to the rise of the tungsten influx. A clear reduction of the carbon content has now become visible. The slow decrease of the C concentration with increasing W coverage can be explained by the strong main chamber recycling. Now, the divertor carbon source contributes significantly to the core C content.

1. Introduction

For the plasma wall interaction, the extrapolation from present day devices towards ITER and beyond is largest, which makes the material choice for the plasma facing components (PFC) a very critical issue. PFCs with low erosion, controllable tritium inventory, high thermo-mechanical stability, good heat transfer properties and stability of these properties under neutron irradiation are required. ITER [1] still follows a conservative approach using beryllium for the main chamber PFCs. In a reactor however, Be will not be a viable solution due to its high erosion yield and high-Z components may have to be used [2,3]. Tungsten as first wall material implies the risk of strong central power losses by impurity radiation, and the tungsten concentration in a reactor has to be kept below a level of $\approx 10^{-4}$. Due to this low concentration limit, active control of the radiation losses in the plasma edge by puffing of low-Z or medium-Z gases (nitrogen, neon or argon) is mandatory to enforce a sufficiently low temperature in the divertor, and thus, maintain conditions with low tungsten erosion yield.

ASDEX Upgrade has pursued a continuous increase of tungsten surfaces during the last seven years. At present, 85% of the PFCs are tungsten coated and only the graphite tiles in the divertor and at some minor parts in the main chamber will have to be exchanged to W-coated tiles during this vent in 2006. The enhancements added in 2005 concentrated on the most critical PFCs receiving the highest particle and energy flux densities in the main chamber: the poloidal limiters of the 4 ICRF antennas, which are a part of the window frame surrounding each antenna, and the guard limiters, which are located at each side of the 2 neutral beam ducts. The coating of these limiters has now been completed after initial tests in 2003-2005, where at first, one guard limiter [4] and subsequently, one ICRF limiter was equipped with W-coated test tiles.

2. Tungsten coatings

Tungsten has an electrical conductivity 200 times larger than that of carbon based materials, which leads to considerably higher load of the support structures due to eddy currents and halo currents if bulk tungsten tiles are used. Reinforcement of the support structures is very costly and time consuming and therefore ASDEX Upgrade has chosen the coating solution. In preparatory experiments using markers [5–8], the erosion at different positions of the PFCs has been evaluated and the thickness and the technique of the coating was chosen accordingly

[9,10]. It turned out that thin coatings ($d < 10\mu$m) could be reliably produced on graphite using physical vapour deposition (PVD) techniques. These thin coatings withstood power loads of more than 15 MWm^{-2} up to melting conditions and showed very good adhesion when produced by plasma arc deposition [11]. They even survived thermal shocks using an ion beam with power loads above 30 MWm^{-2} for 0.3 s, which are expected at the dump regions of the neutral beam injection in case of failure of the primary protection circuits. W coatings on graphite (SGL Carbon R6710) were more reliable than on CFC (Dunlop DMS 704), which can be attributed to the very inhomogeneous surface characteristics and the strong mismatch of thermal expansion coefficients depending on the fibre orientation of the CFC.

Long term marker measurements at the strike point region of the lower divertor, which were performed in the last campaign, yielded a W erosion of $\geq$0.2 nms^{-1}. Therefore thicker coatings are foreseen for the divertor, similar to the ones used in the ASDEX Upgrade W divertor experiment [12]. W coatings ($d = 200\mu$m) on graphite (SGL Carbon R6710 and Schunk FP479) were produced by vacuum plasma spray (VPS). After initial problems and defects occurring at test tiles used at the low field side auxiliary limiters, reliable coatings were independently developed by Plansee and Sulzer-Metco. At the ion beam test facility GLADIS, they passed successfully thermal screening with power loads up to 22 MWm^{-2} as well as cyclic loading at 10 MWm^{-2} [13].

In comparison to C-based PFCs, the W surfaces exhibit a larger storage of He during He glow discharge cleaning (HeGD) and thus a larger release of the stored He during the next discharges. Laboratory experiments have investigated this effect in more detail [14]. For the plasma operation, the frequency and duration of HeGD, which used to be performed after each discharge, has been reduced to control the He content [15].

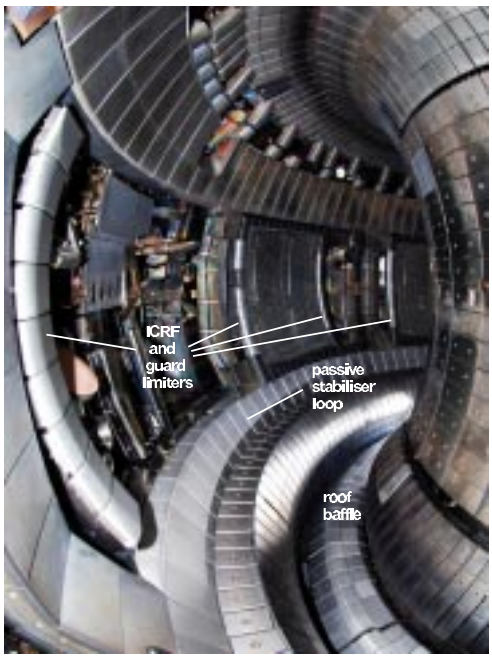

Figure 1: *View into the ASDEX Upgrade vacuum chamber. All major PFC, except the strike point region of the lower divertor are W coated. The most recently installed W-coated PFCs are indicated.*

3. Evolution of intrinsic impurities

3.1. Tungsten W concentrations (c_W) are routinely extracted from spectroscopic measurements [16]. Fig. 2 shows the distribution of W concentrations, taken during time intervals of sufficiently constant plasma parameters for the last campaign with the new W-based limiters and the two previous campaigns with only the central column as major W source in the main chamber. Here, c_w is determined from emission lines radiating at T_e=1–1.5 keV, i.e. at about r/a=3/4 for the majority of discharges. W transport is the main parameter determining the central W concentration [16–18], which obscures the source effect and yields a wide distribution of c_W over more than 4 orders of magnitude. Strongly accumulating discharges, where the 1 keV emission shifts to the plasma centre, have been disregarded in order to partly exclude the central transport effects. Two cuts of the data with (red/gray) and without (black) considerable ICRF heating are shown, and mean values are indicated as bars of same colour. Without ICRF the distributions are very similar, while with ICRF the mean value of c_w is increased by about a factor of 5 in the last campaign and only by a factor of 2 in the previous campaigns. ICRF strongly increases the limiter W-source as shown below. The mean value of c_w with ICRF in the last campaign is about 10^{-5}.

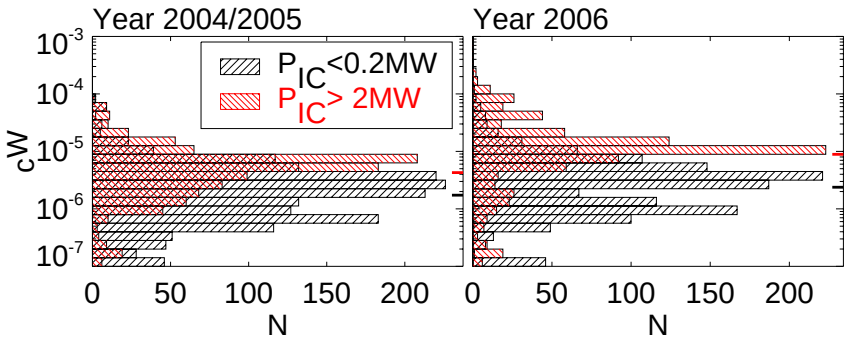

Figure 2: *Distributions of tungsten edge concentration with(red) and without(black) considerable ICRF heating for the campaign 2006 with tungsten limiters in comparison to two previous campaigns with graphite limiters. Bars at the right hand side give mean values.*

3.2. Carbon Despite a major fraction of the main chamber recycling takes place on the inner heat shield [19], its coating with tungsten did not lead to a significant reduction of the carbon content and recycling fluxes. However, during the last campaign, a clear reduction of the carbon concentration (c_C) became apparent. A numerical code has been set up to describe the carbon particle transport and migration pattern, where the carbon sputtering yield on the W-surfaces is assumed to follow a linear dependence on deposition thickness for thin carbon layers [20]. A specified carbon erosion flux from the outer divertor can be fed to the upstream separatrix in the model to simulate the effect of a net outer divertor carbon source. The amount of deuterium gas puff in the calculations is adjusted so as to be equal to the pumped flux derived from ionisation gauge measurements in the pump chamber and the known pumping speed [21]. Only conditions with small net wall pumping or gas release are taken into account. For a typical experimental situation, a deuterium atom recycles about 3-5 times before it is pumped. Since carbon is entrained in the deuterium flux, this recycling pattern is mainly responsible for the build-up of a thin carbon layer on the W-surfaces with a thickness below two monoatomic layers.

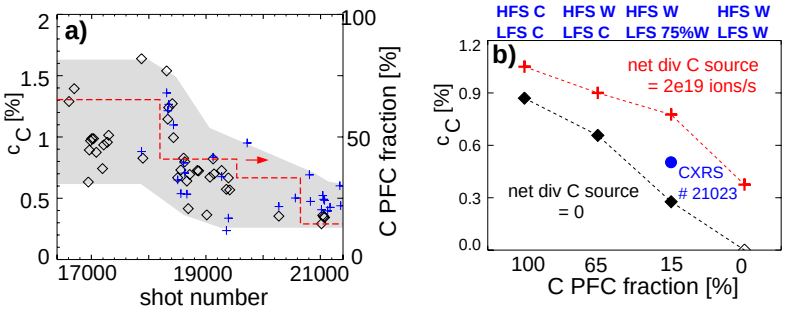

Figure 3: *a) Long term development of the carbon concentration in the outer core plasma during a high density standard H-mode phase as measured by CXRS with NBI injector 1 (diamonds) and 2 (crosses). The dashed lines indicate the fraction of PFC carbon coverage. b) Modelling of the C concentration resulting from HFS and LFS fluxes with changing W coating in AUG with and without net C ion influx from the divertor. Conditions correspond to a).*

Figure 3(a) shows the long term development of c_C during the high density phase of a standard H-mode discharge [22] performed routinely, together with the carbon PFC coverage fraction for the corresponding campaign. There are considerable variations of c_C due to boronisation, diagnostic imperfections etc., but a clear trend towards lower carbon concentrations for the most recent discharges is significant. Results of the particle transport model for these discharge conditions are shown in Fig.3(b) for different carbon PFC fractions and the corresponding components indicated on top. Diamonds denote values of c_C without divertor carbon source, crosses with a net source of 2×10^{19} ions/s delivered at the upstream separatrix. A typical concentra-

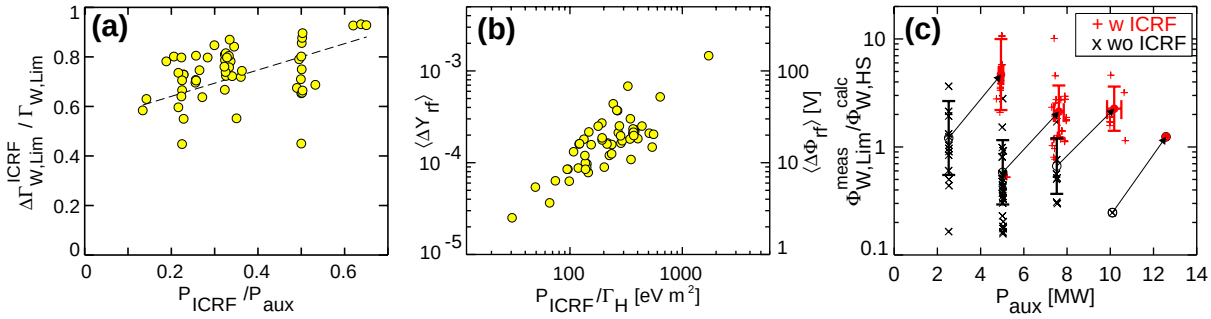

Figure 4: *(a): Increase of W influx from all LFS limiters due to ICRF is shown as a function of the ICRF power fraction. The line is drawn to guide the eye. (b): Mean difference of the effective yields* $\langle \Delta Y_{rf} \rangle$ *and according increase of the sheath potential* $\langle \Delta \Phi_{rf} \rangle$ *at the ICRF limiter versus the ratio of ICRF power and hydrogen recycling flux density* P_{ICRF}/Γ_H*. (c): Ratio of the W source at the LFS limiters over that at the heat shield* ($\Phi^{meas}_{W,Lim}/\Phi^{calc}_{W,HS}$) *during ICRF+NBI and NBI only as a function of the total auxiliary heating power. The limiter influx is measured whereas the influx from the heat shield is derived from the measured C influx using a sputtering yield of 1%.*

tion measured by CXRS is indicated as circle. The trend of C reduction compares well with Fig.3(a) if a net carbon influx of $\approx 10^{19}$ atoms/s from the outer divertor is assumed. The model nicely reproduces the observation that W coating of the inner heat shield, where 2/3 of the main chamber recycling occurs, only slightly decreases c_C. Further information about the net divertor carbon source could be obtained from the behaviour after a boronisation. Here, 1.5×10^{19} C ions/s was used to reproduce the recovery of c_C in an H-mode discharge with slightly lower density compared to Fig.3(a) [20].

4. Tungsten Influxes

Special emphasis was put on the investigation of the W sources, especially during ICRF [23,24]. Fifteen lines-of-sight are used to measure influx profiles along the limiter height. The set-up allows the simultaneous measurement of the W I line at 400.8 nm, a B II at 412.3 nm and the Balmer-δ transition at 410.1 nm. The newly installed back-illuminated frame-transfer CCD camera increases strongly the temporal resolution enabling ELM resolved influx measurements. The measured photon fluxes are transformed into ion fluxes using photon efficiencies (S/XB). Effective sputtering yields Y_{eff} are calculated by dividing the W flux density by the deuterium flux density.

4.1. ICRF induced tungsten influx When ICRF heating is switched on/off, the tungsten influx at the limiters of the active ICRF antennas strongly increases/decreases with a rise/decay time below 1 ms. The increase is strongest at the active antenna but also visible at the neighbouring guard limiter at a toroidal distance of ≈0.8 m and at the opposite ICRF limiter at a distance of ≈5 m [25]. A similar behaviour has been reported from the all-molybdenum device Alcator C-Mod when operating with Mo ICRF limiters [26]. On the ICRF limiter, ICRF was found to cause up to a factor of 65 higher local W influx densities per heating power than NBI. The ICRF contribution to the total limiter influx was estimated by comparing ICRF on/off phases during a number of discharges and is shown in Fig. 4(a) versus the ICRF heating power fraction. The ICRF induced fraction rises with the power fraction reaching values of $> 90\%$ already at $P_{ICRF}/P_{aux} = 0.5$. Even more strikingly already for the lowest ICRF power fractions, the ICRF induced W influx dominates.

The fast temporal response and the spatial structure rules out a predominant contribution of ICRF induced fast ions to the W erosion and points towards the sheath rectification effect as main reason to the increased W influx. The additional average sheath potential $\Delta\Phi_{rf}$ accel-

erates the sputtering ion onto the target which leads to an increased erosion yield. For a D^+ plasma with an admixture of 1% C^{4+}, synonymous with the mixture of light impurity ions, the difference of the effective yields ΔY_{rf} with and without additional sheath potential is only weakly dependent on the edge temperature and for $\Delta\Phi_{rf}$ between 1 V and 1 kV, it is roughly $\Delta\Phi_{rf}$ [V] = 10^5 ΔY_{rf}. ΔY_{rf} can be determined from consecutive time slices with/without ICRF during a discharge and serves as a simple estimate of the sheath potential increase. For H-mode discharges with type-I ELMs heated by NBI and ICRF, Fig. 4(b) shows the mean sheath potential increases at the ICRF limiter, which approximately fill the range 1-100 V. The data set is shown versus P_{ICRF}/Γ_H since $\Delta\Phi_{rf}$ increases with ICRF power and decreases with the hydrogen recycling level. The uncertainty of ΔY_{rf} is estimated to be a factor of 4. Scans of the safety factor q were performed. By varying the edge-q the angle between the field lines and Faraday screens is changed. Depending on the details of the plasma shape, they are nearly parallel for $q_{95} \approx 3$ and lowest electrical fields are expected in this case. However, even for different combinations of B_t and I_p (performed in the upper divertor) no significant change of the W influx is found.

In terms of their active area of ≈ 0.3 m^2, the LFS limiters represent only a minor fraction of the W PFCs. However, due to the large flux densities, the W source is easily measurable. In contrast, the area of the central heat shield (HS) is much larger (an active area of 8.4 m^2 is taken for the assessment), but the W-flux densities are barely measurable. In order to get hold of the W-flux from the heat shield $\Phi^{calc}_{W,HS}$, the measured C flux density is integrated over the whole area and multiplied with the W erosion yield by C of $Y^C_W = 10^{-2}$ representing the yield of C^{3+} at $T_e = 10$ eV. Fig. 4(c) shows the ratio of the measured W influx from the LFS limiters to the calculated W influx from the heat shield for different P_{aux}. Without ICRF heating, the typical ratio is in the range of 1. With ICRF, the ratio increases by a factor 2-10. For the highest auxiliary heating powers, the relative importance of the limiters seems to decrease, however, the assessment of the heat shield source is too rough for a detailed interpretation.

4.2. Tungsten influx due to fast NBI ions A fraction of the fast D^+ ions from the neutral beam injection (NBI) heating is transported onto the limiters during the slowing down process and causes sputtering of tungsten. The loss probability for a fast ion increases with decreasing radial distance to the plasma edge and decreasing velocity fraction along the magnetic field direction ($v_{||}/v$), i.e. increasing pitch angle. The eight beam sources at ASDEX Upgrade have different beam geometries, and the fast ions are born with an average pitch angle of $\langle v_{||}/v\rangle \approx 0.2$ for the most radial beam and $\langle v_{||}/v\rangle \approx 0.7$ for the most tangential beam.

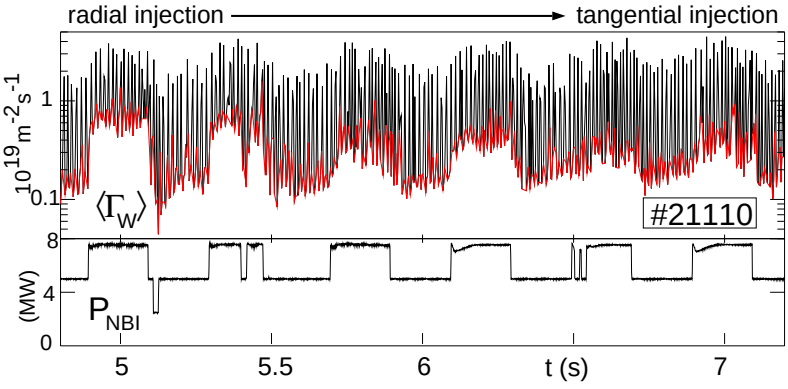

Figure 5: *Spatially averaged tungsten influx from an ICRF limiter during a scan of different NBI sources added to a steady 5 MW NBI heating (f_{ELM}=76 Hz, ΔR_{sep}=4 cm). The radial beams are followed by the tangential beams.*

Type-I ELMy H-mode discharges with constant heating by 2 NBI sources ($\langle v_{||}/v\rangle \approx 0.46$) were performed, where each 400 ms one of the remaining 6 sources was added for a duration of 200 ms. Fig.5 shows the variation of the average tungsten influx $\langle\Gamma_W\rangle$ on all six channels of one ICRF limiter during the scan of the additional

beam sources, which starts with the most radial beam and ends with the most tangential beam. The rapid fluctuations are due to type-I ELMs which had a frequency f_{ELM}=76 Hz. The scans was repeated at two distances between separatrix and limiter of ΔR_{sep}=4 cm and 5 cm and at a higher deuterium puff level, which increased the ELM frequency to 150 Hz. The sputtering caused by each source was evaluated by taking the difference of the influx densities with and without the additional beam. Fig.6(a) displays the temporal mean of these differences $\langle\Gamma_W\rangle$-$\langle\Gamma_W^0\rangle$ versus $\langle v_{||}/v\rangle$ of each beam. The limiter W-erosion is clearly enhanced for the more radial beams compared to the tangential beams.

Monte Carlo code calculations have been performed to model the fast particle load and the respective tungsten erosion rates at the limiters in detail. The start position and velocities of the fast NBI ions were calculated with the Monte Carlo code FAFNER [27]. Subsequently, the orbit of the gyro centre of the ions was calculated including pitch angle scattering, slowing down collisions and magnetic field ripple. The modelling results are overlaid as lines in Fig.6(a). Without magnetic field ripple, the calculated erosion fluxes are much to low. With ripple and pure collisional fast ion transport, the calculated fluxes agree quite well with the experiment, however, the code predicts a stronger decay of the limiter erosion with increasing $\langle v_{||}/v\rangle$ than experimentally observed. The weaker experimental decay is due to the transport induced by ELMs, which could be temporally resolved in the low frequency case. In Fig.5 the lower influx envelope (marked red) shows a much stronger dependence on the beam source than the ELM peaks. In Fig.6(b), the different contributions during and in-between ELMs are separately displayed. In the high ELM frequency case, the spectroscopic time resolution is not sufficient to resolve the ELMs, however, the time averaged signals in Fig.6(a) are identical in the two cases. Thus, the effect of each ELM on the W erosion decreases with increasing ELM frequency as is usually observed for the loss of plasma energy. The ELM is expected to cause a limiter load in the fast ion channel as well as in the thermal channel. For the larger separatrix distance ΔR_{sep}=5 cm, the erosion by thermal impurity ions has been estimated to be small against the fast ion erosion, such that the weaker decay with $\langle v_{||}/v\rangle$ is attributed to an ELM induced fast ion loss [23].

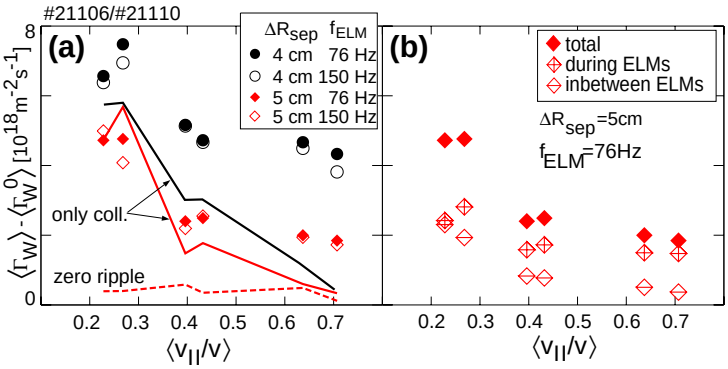

Figure 6: *In (a), spatially and temporally averaged change of tungsten influx is shown versus $\langle v_{||}/v\rangle$ of each additional NBI source for two ELM frequencies and two distances between separatrix and limiter. The solid lines give the modelling results with pure collisional fast ion transport, while the dashed line shows a case without magnetic field ripple. In (b), the different contributions in-between and during ELMs are displayed for a low ELM frequency case.*

4.3. Effect of ELMs A few discharges were measured with high time resolution of 253 μs on a single line-of-sight to resolve single type-I ELMs. The ELM frequency varied between 46 to 175 Hz and the ELM energy W_{ELM} decreased from 25 to 6.7 kJ with an approximate $1/f_{ELM}$ dependence. Each ELM causes a drastic increase of the tungsten influx by more than an order of magnitude. In Fig.7(a), the tungsten fluence during an ELM is seen to rise approximately linear with W_{ELM} for a set of purely NBI heated plasmas (5-7.5 MW) and with a 3 times larger slope for a set with additional ICRF heating of 0.7 MW per antenna. The increased W influx

during ELMs is mainly due to a strong increase of the effective sputtering yield as can be seen in Fig.7(b). Here, Y_{eff} is shown for the phases inbetween ELMs and during ELMs. The ELM values are a temporal average during the whole ELM, i.e. the ratio of the tungsten and hydrogen fluences. Y_{eff} rises by about a factor of 10 during the ELMs for pure NBI heating and less for the few points with ICRF (ICRF does not switch off during ELMs), which have higher Y_{eff} between ELMs. This rise reflects an increased mean energy of the ions hitting the W-surface, which is probably due to an increase of the edge temperature as well as an increase of the fast ion load onto the limiters. For the whole data set including the ICRF points, the fraction of the W fluence during ELMs to the total fluence during and in-between ELMs does not dependend on the ELM size and is (70±10)%. It has to be noted, that these data give only the local behaviour at one position in the middle of the ICRF limiter and not the changes of the global influx from all limiters. The effect of ELMs was also measured for the influx of the low-Z elements boron and carbon. The influx during ELMs changes much less and the ELM contribution to the total influx is only 45±5%.

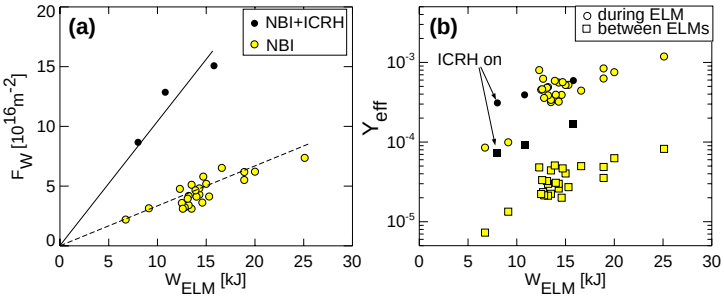

Figure 7: *(a) shows the tungsten fluence F_W during type-I ELMs in the middle of an ICRF limiter versus the ELM energy loss of the plasma W_{ELM} for discharges with NBI heating and additional ICRF heating. For the same data set, (b) depicts the effective tungsten yield during and in-between ELMs.*

4.4. Boronisations Boronisations are regularly performed (after about 200 discharges) in order to permit a broad range of experiments, which partly are orthogonal to the requirements identified for low tungsten erosion, e.g. experiments with low edge densities, counter NBI, etc.. These experiments are grouped right after boronisations. Boronisations strongly reduce the impurity level in ASDEX Upgrade. Oxygen plays only a significant role shortly after a major vent [15]. In contrast, the content of medium-Z impurities such as Fe and Cu, which are also existent in the plasma (see for example [28]), as well as W are strongly suppressed (1-2 orders of magnitude) under otherwise similar conditions. For the W-influxes from the ICRF limiters, the reduction is very transient and decays within 20 discharges. This observation is in line with estimates taking into account the measured hydrogen flux and an effective boron erosion yield below 1% at the ICRF limiter. For the guard limiters the time-constant is considerably larger reflecting the smaller load. The W density recovery in the main plasma occurs on an intermediate timescale [29].

5. Conclusions

In the last campaign ASDEX Upgrade was equipped with an area of about 36 m^2 of W coated tiles. The main, newly added components were the low field side poloidal guard limiters, the roof baffle in the lower divertor and the lower passive stabilizer loop. The elimination of all uncoated graphite tiles is foreseen for the campaign in 2007. Thick VPS coatings (200 μm) have been successfully tested and will be ready for installation.

The increased W-area resulted in higher W concentrations in the plasma. Especially the LFS limiters represent a significant W source mainly during ICRF operation. ICRF leads to an enhancement of the erosion yields from impurity ions, which is probably due to a rise of the sheath potential. This behaviour makes the balance of the heating methods more delicate and

suggests a preferential use of ECRH for central heating. NBI leads to sputtering by fast D^+ ions. The fast ion loss is enhanced by ELMs. Code calculation of the fast ion sputtering are in good agreement with the measurements. In H-modes with type-I ELMs, about 70% of the local W-influx at the middle of an ICRF limiter appears during ELMs indepenent of the ELM frequency. During the ELM, the mean energy of the ions hitting the W-surface is increased, which is the predominant contribution to the rise of the tungsten influx.
A clear reduction of the carbon content has now become visible. The slow decrease of the C concentration can be explained by the strong main chamber recycling. Additionally, it was found that the divertor carbon source contributes significantly to the core C content. The planned ITER PFC material choice is quite similar to the present AUG conditions, with carbon mainly left at the strike point zones in the divertor. The observed migration of carbon out of the divertor and through the main chamber in AUG calls for further predictive work for ITER to asses the concomitant tritium co-deposition.

References

[1] AYMAR, R. et al., Plasma Phys. Controlled Fusion **44** (2002) 519.
[2] JANESCHITZ, G. et al., Nucl. Fusion **40** (2000) 1197 .
[3] BOLT, H. et al., J. Nucl. Mater. **329-333** (2004) 66.
[4] DUX, R. et al., J. Nucl. Mater. **337-339** (2005) 852.
[5] NAUJOKS, D. et al., J. Nucl. Mater. **210** (1994) 43.
[6] KRIEGER, K. et al., J. Nucl. Mater. **266–269** (1999) 207.
[7] KRIEGER, K. et al., J. Nucl. Mater. **337-339** (2005) 10.
[8] MAIER, H. et al., J. Nucl. Mater. **335** (2004) 515.
[9] GARCÍA-ROSALES, C. et al., Fusion Tech. **32** (1997) 263.
[10] MAIER, H. et al., J. Nucl. Mater. **307-311** (2002) 116.
[11] MAIER, H. et al., Surface and Coating Technology **142-144** (2001) 733.
[12] NEU, R. et al., J. Nucl. Mater. **241–243** (1997) 678.
[13] NEU, R. et al., submitted to Physica Scripta (2006).
[14] SCHMID, K. et al., 21st IAEA-FEC, Chengdu, China (2006) EX/3–3Rb.
[15] ROHDE, V. et al., PSI 2006, Hefei, submitted to J. Nucl. Mater. (2006).
[16] NEU, R. et al., Nucl. Fusion **45** (2005) 209.
[17] DUX, R. et al., 20th IAEA-FEC, Vilamoura, Portugal (2004), IAEA–CN–116/EX/P6–14.
[18] KALLENBACH, A. et al., Plasma Phys. Controlled Fusion **47** (2005) B207.
[19] KALLENBACH, A. et al., Nucl. Fusion **43** (2003) 573.
[20] KALLENBACH, A. et al., PSI 2006, Hefei, submitted to J. Nucl. Mater. (2006).
[21] KALLENBACH, A. et al., Plasma Phys. Controlled Fusion **46** (2004) 431.
[22] RYTER, F. et al., Plasma Phys. Controlled Fusion **44** (2002) A407.
[23] DUX, R. et al., PSI 2006, Hefei, submitted to J. Nucl. Mater. (2006).
[24] BOBKOV, V. et al., PSI 2006, Hefei, submitted to J. Nucl. Mater. (2006).
[25] DUX, R. et al., 32nd EPS Conf. on Plasma Physics, Tarragona, (2005) P–1.010.
[26] LIPSCHULTZ, B. et al., PSI 2006, Hefei, submitted to J. Nucl. Mater. (2006).
[27] LISTER, G., Tech. Report IPP 4/222, MPI für Plasmaphysik, Garching, Germany, 1985.
[28] SCHUSTEREDER, V. et al., PSI 2006, Hefei, submitted to J. Nucl. Mater. (2006).
[29] NEU, R. et al., PSI 2006, Hefei, submitted to J. Nucl. Mater. (2006).